IEEE Transactions on Automation Science and Engineering (T-ASE) paper, presented at ICRA 2026, Vienna, Austria.
Cite as T-ASE paper.

A Near-Time-Optimal Trajectory Planning Under Torque and Jerk Constraints for Industrial Robots on Fixed Paths

Shize Zhao, Tianjiao Zheng, Chengzhi Wang, Yanhe Zhu, and Jie Zhao

***Abstract*—Trajectory planning plays a pivotal role in robotic motion planning, particularly in achieving time-optimal motion under complex dynamic constraints. Although the Time-Optimal Path Parameterization (TOPP) algorithm effectively addresses trajectory generation under joint torque constraints, classical methods often overlook third-order constraints. As a result, the generated trajectories, while torque-feasible, exhibit excessive jerk and poor dynamic stability, which limits their practical applicability. To overcome these limitations, this paper proposes a trajectory planning framework that simultaneously enforces torque and jerk constraints. Building upon torque-constrained TOPP, the method integrates a shooting-based strategy to identify switching points through bidirectional integration under jerk constraints and employs a Sigmoid-based fusion scheme to eliminate integration errors and ensure smooth transitions. The proposed approach is experimentally validated on a six-degree-of-freedom industrial robot. Comparative evaluations with the TOPP-RA algorithm demonstrate that the method significantly reduces both high-frequency vibrations during high-speed execution and residual oscillations after motion termination. Feedback from torque rate measurements, vibration sensors, and laser tracker data confirms faster settling and improved compliance, making the approach well-suited for complex industrial scenarios.**

***Note to Practitioners*—In welding, assembly, and high-speed transport, robots must follow fixed paths quickly while minimizing vibration, since excessive oscillations reduce accuracy and shorten component lifespan. Conventional trajectory planners seldom enforce jerk limits, leading to abrupt torque reversals and residual vibrations. This work introduces a method that simultaneously accounts for torque and jerk constraints, enabling near time-optimal trajectories that remain smooth and dynamically stable. Experiments on a six-axis industrial robot demonstrate reduced vibration, faster post-motion settling, and improved compliance. A current limitation is the reliance on precise knowledge of dynamic limits, which may restrict deployment in uncertain environments. Future work will explore data-driven adaptation under real operating conditions to broaden industrial applicability.**

***Index Terms*—Time-optimal trajectory planning, torque constraints, jerk constraints, shooting method, sigmoid-based smoothing.**

I. Introduction

INDUSTRIAL robots are increasingly deployed in high-speed and high-precision applications such as welding, spraying, and assembly, where smooth and rapid execution along predefined paths is essential [1], [2], [3], [4]. In real applications, however, the execution quality of such motions can be severely affected by external disturbances and dynamic uncertainties, whose influence is often amplified when the robot operates at high speeds or undergoes abrupt variations in motion [5], [6], [7]. These factors impose additional demands on trajectory generation and make accurate execution more challenging. To achieve high dynamic performance, trajectory planners must therefore generate time-efficient motion profiles that enable precise and stable tracking of complex paths [8]. This optimization is fundamentally constrained by the robot's physical limits. In particular, joint velocity and torque bounds directly restrict actuator capabilities and must be explicitly considered during motion planning [9].

Time-Optimal Path Parameterization (TOPP) is a well-established framework for generating time-efficient trajectories along a fixed geometric path under dynamic constraints [10]. Existing solutions to the TOPP problem typically fall into three categories: (1) dynamic programming, which discretizes the $(s, \dot{s})$ domain and applies recursive optimization to determine the switching structure [11], [12]; (2) convex optimization, which formulates the problem as a tractable convex program after discretizing the path [13]; and (3) numerical integration based on Pontryagin's Maximum Principle, which derives bang–bang acceleration profiles through forward–backward integration [14]. In practice, however, time-optimal trajectories generated under second-order constraints may deviate significantly from the intended motion due to external interaction forces, frictional effects, or severe jerk-induced vibrations.

Although certain interaction-aware models account for torque variations produced by external forces and viscous friction [15], most existing TOPP approaches focus primarily on second-order constraints such as joint torque or acceleration, while overlooking third-order dynamic characteristics. As a result, the generated trajectories often exhibit discontinuities in

Received 4 September 2025; revised 20 November 2025; accepted 8 December 2025. Date of publication 11 December 2025; date of current version 12 January 2026. This article was recommended for publication by Associate Editor C. M. Abdissa and Editor H. Moon upon evaluation of the reviewers' comments. This work was supported in part by the National Key Research and Development Program of China under Grant 2022YFB4700300, in part by the National Natural Science Foundation of China under Grant 52025054 and Grant 52435001, and in part by the Self-Planned Task of the State Key Laboratory of Robotics and Systems [Harbin Institute of Technology (HIT)] under Grant SKLRS2023KF18 and Grant SKLRS202401A01. *(Corresponding authors: Tianjiao Zheng; Yanhe Zhu.)*

The authors are with the School of Mechatronics Engineering, Harbin Institute of Technology, Harbin 150001, China (e-mail: zhengtj@hit.edu.cn; yhzhu@hit.edu.cn).

This article has supplementary downloadable material available at https://doi.org/10.1109/TASE.2025.3642937, provided by the authors.

Digital Object Identifier 10.1109/TASE.2025.3642937

IEEE Transactions on Automation Science and Engineering (T-ASE) paper, presented at ICRA 2026, Vienna, Austria.

acceleration near switching points, giving rise to pronounced jerk spikes. These discontinuities frequently manifest as sudden torque reversals that may excite structural resonances and induce mechanical vibrations. Such effects can damage actuators and transmission components and may also lead to large tracking errors. Consequently, despite being theoretically optimal, bang–bang trajectories are often difficult to execute reliably on physical robotic systems [16], [17].

Incorporating jerk constraints substantially increases the complexity of trajectory planning. Enforcing bounds on the third derivative of the path parameter $s(t)$ expands the state representation to $(s, \dot{s}, \ddot{s})$, and requires identifying transitions not only between torque-limited and jerk-limited phases but also among jerk phases themselves [18]. Direct numerical integration becomes challenging in this high-dimensional, hybrid-constrained landscape and may require considerable computational effort without guaranteeing optimality. Furthermore, the presence of jerk constraints introduces intrinsic nonconvexity, preventing straightforward application of conventional convex optimization techniques [19], [20].

To address these challenges, prior research has proposed several approximation techniques to incorporate higher-order constraints into time-optimal path parameterization. Palleschi et al. [21] employ McCormick envelope relaxations to convexify jerk (acceleration-derivative) constraints, enabling efficient convex approximations of these higher-order bounds. Huang et al. [22] develop a sampling-based formulation that enforces acceleration and jerk limits on discretized path grids. Although these approaches effectively incorporate higher-order kinematic constraints, they do not explicitly account for joint-space torque feasibility during the parameterization process.

In addition to such direct convexification and sampling-based strategies, other studies enhance computational tractability by reformulating jerk constraints into representations that can be handled within convex or sequentially convex optimization frameworks. Ma et al. [23] convert jerk limits into equivalent linear acceleration bounds, thereby enabling indirect enforcement within convex programs. Debrouwere et al. [24] express nonconvex jerk constraints as difference-of-convex functions and address them using sequential convex programming (SCP). However, such reformulation-based approaches typically require solving multiple convex subproblems, and their path-parametric enforcement of jerk bounds becomes computationally demanding when applied to full joint-space dynamics. Taken together, these methods indicate that achieving time-optimal trajectory planning under simultaneous torque and jerk constraints remains a challenging open problem, particularly for complex manipulator trajectories.

To overcome the above limitations, this paper introduces a trajectory planning framework that enables time-efficient motion along complex end-effector paths while simultaneously satisfying joint torque and jerk constraints. Prior studies [25], [26] have shown that appropriate path preprocessing can reduce the discontinuities that commonly occur at acceleration–deceleration switching points in TOPP-based approaches. Building on this insight, we first compute a torque-feasible baseline trajectory through a convex optimization formulation, and subsequently address the residual jerk-related discontinuities associated with bang–bang switching. Dense resampling is applied in critical regions, followed by bidirectional shooting under bounded jerk constraints to identify feasible transitions between torque-limited and jerk-limited motion phases. A sigmoid-based fusion mechanism is then employed to smoothly reconcile the forward and backward integrations, ensuring trajectory continuity while avoiding artifacts introduced during refinement. The resulting trajectory satisfies both torque and jerk bounds while maintaining time efficiency, enabling smooth and dynamically consistent execution on industrial robotic manipulators.

The remainder of this paper is organized as follows. The Preliminaries section introduces the problem formulation, including the modeling of joint torque and jerk constraints. The Method section presents the proposed hybrid trajectory planning framework, covering torque-feasible baseline generation, bounded-jerk integration strategies, and the fusion mechanism. The Experiments section reports evaluation results on a six-degree-of-freedom industrial robot, comparing the proposed method with existing approaches based on joint torque measurements, vibration sensing, and laser tracking data. Finally, the Conclusion section summarizes the key findings of this study.

II. Preliminaries

This section presents the mathematical foundation for trajectory planning of industrial manipulators under joint torque and jerk constraints along a predefined end-effector path. The central challenge lies in path-parameterizing a fixed geometric path such that the resulting velocity profile is dynamically feasible and time-optimal.

A. TOPP Under Joint Torque Constraints

For an n-DOF robotic system, its configuration in joint space is denoted by a vector $\mathbf{q} \in \mathbb{R}^n$. Assuming the manipulator is fully actuated, its dynamics can be described by:

$$\mathbf{M}(\mathbf{q})\ddot{\mathbf{q}} + \dot{\mathbf{q}}^\top \mathbf{B}(\mathbf{q})\dot{\mathbf{q}} + \mathbf{f}(\mathbf{q}) = \boldsymbol{\tau} \tag{1}$$

Here, $\mathbf{M}(\mathbf{q}) \in \mathbb{R}^{n\times n}$ is the inertia matrix, $\mathbf{B}(\mathbf{q}) \in \mathbb{R}^{n\times n}$ accounts for Coriolis and centrifugal effects, and $\mathbf{f}(\mathbf{q}) \in \mathbb{R}^n$ represents gravitational and Coulomb friction terms. The vectors $\dot{\mathbf{q}}, \ddot{\mathbf{q}} \in \mathbb{R}^n$ are the joint velocity and acceleration, and $\boldsymbol{\tau} \in \mathbb{R}^n$ is the control torque.

A geometric path in configuration space is defined as $\mathbf{q}(s), s \in [0, s_{\text{end}}]$. The path parameterization is given by a strictly increasing scalar function $s(t) : [0, t_{\text{end}}] \to [0, s_{\text{end}}]$. Using the chain rule, the joint velocity and acceleration can be expressed as:

$$\dot{\mathbf{q}} = \mathbf{q}'(s)\dot{s}, \quad \ddot{\mathbf{q}} = \mathbf{q}''(s)\dot{s}^2 + \mathbf{q}'(s)\ddot{s} \tag{2}$$

Substituting Eq. (2) into Eq. (1), the manipulator dynamics can be reformulated in terms of the path parameter s:

$$\mathbf{a}(s)\ddot{s} + \mathbf{b}(s)\dot{s}^2 + \mathbf{c}(s) = \boldsymbol{\tau} \tag{3}$$

IEEE Transactions on Automation Science and Engineering (T-ASE) paper, presented at ICRA 2026, Vienna, Austria.

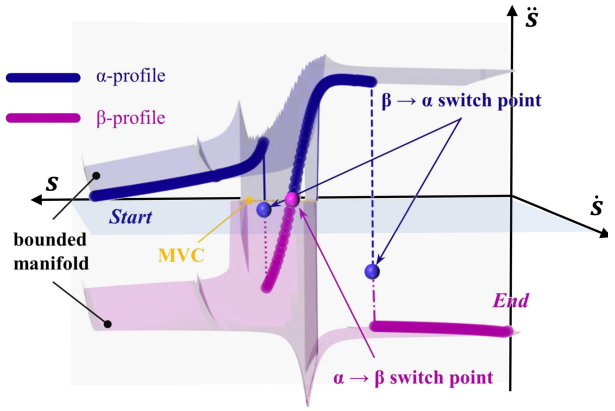

Fig. 1. Three-dimensional visualization of the time-optimal trajectory on a fixed path under torque constraints. The horizontal axes represent the path position s and path velocity $\dot{s}$, while the vertical axis indicates path acceleration $\ddot{s}$. The admissible region (bounded manifold) is bounded by the $\alpha(s,\dot{s})$ (maximum feasible acceleration, blue) and $\beta(s,\dot{s})$ (minimum feasible acceleration, purple). The trajectory starts at the initial state and follows the acceleration-constrained α-profile, switches at an $\alpha \to \beta$ switch point, decelerates along the β-profile, and completes at the target state.

with the coefficient vectors defined as:

$$\begin{aligned}\mathbf{a}(s) &= \mathbf{M}(\mathbf{q}(s))\mathbf{q}'(s),\\ \mathbf{b}(s) &= \mathbf{M}(\mathbf{q}(s))\mathbf{q}''(s) + \mathbf{q}'(s)^{\top}\mathbf{B}(\mathbf{q}(s))\mathbf{q}'(s),\\ \mathbf{c}(s) &= \mathbf{f}(\mathbf{q}(s))\end{aligned}$$

Introducing the state variable $x = \dot{s}^2$ and control input $u = \ddot{s}$, Eq. (3) becomes a linear form:

$$\mathbf{a}(s)u + \mathbf{b}(s)x + \mathbf{c}(s) = \boldsymbol{\tau} \tag{4}$$

Assuming torque bounds for each joint, the following inequality must be satisfied:

$$\tau_i^{\min} \le a_i(s)u + b_i(s)x + c_i(s) \le \tau_i^{\max} \tag{5}$$

From this, the admissible range of acceleration $\ddot{s}$ for each joint can be computed [14]:

- If $a_i(s) > 0$, then $\beta_i = \frac{-b_i(s)x - c_i(s) + \tau_i^{\min}}{a_i(s)} \le \ddot{s} \le \alpha_i = \frac{-b_i(s)x - c_i(s) + \tau_i^{\max}}{a_i(s)}$
- If $a_i(s) < 0$, then $\beta_i = \frac{-b_i(s)x - c_i(s) + \tau_i^{\max}}{a_i(s)} \le \ddot{s} \le \alpha_i = \frac{-b_i(s)x - c_i(s) + \tau_i^{\min}}{a_i(s)}$

The overall feasible acceleration interval at state $(s,\dot{s})$ is:

$$\alpha(s,\dot{s}) = \min_i \alpha_i(s,\dot{s}), \quad \beta(s,\dot{s}) = \max_i \beta_i(s,\dot{s}) \tag{6}$$

As illustrated in Fig. 1, the admissible region lies between the $\alpha(s,\dot{s})$ and $\beta(s,\dot{s})$ curves. A trajectory $\mathbf{q}(s)$ satisfies the torque constraints if and only if it remains entirely within this bounded region:

$$\beta(s,\dot{s}) \le \ddot{s} \le \alpha(s,\dot{s}) \tag{7}$$

In particular, when $\alpha(s,\dot{s}) < \beta(s,\dot{s})$, Eq. (7) cannot be satisfied, implying the current velocity is infeasible. The Maximum Velocity Curve (MVC) at each s is:

$$\mathrm{MVC}(s) = \min\{\dot{s} \ge 0 \mid \alpha(s,\dot{s}) = \beta(s,\dot{s})\} \tag{8}$$

B. TOPP Under Joint Jerk Constraints

In addition to torque, jerk must also be constrained to ensure smooth and dynamically feasible trajectories. Using the chain rule, the joint jerk along a path-parameterized trajectory can be expressed as:

$$\dddot{\boldsymbol{q}} = \boldsymbol{q}'''(s)\,\dot{s}^3 + 3\boldsymbol{q}''(s)\,\ddot{s}\dot{s} + \boldsymbol{q}'(s)\,\dddot{s} \tag{9}$$

Here, $\mathbf{q}'''(s)$ is the third derivative of joint configuration with respect to the path parameter s, and $\dddot{s}$ denotes the third-order derivative of s with respect to time, i.e., the path jerk. The joint jerk must lie within specified bounds:

$$\boldsymbol{j}_{\min} \le \boldsymbol{q}'''(s)\,\dot{s}^3 + 3\boldsymbol{q}''(s)\,\ddot{s}\dot{s} + \boldsymbol{q}'(s)\,\dddot{s} \le \boldsymbol{j}_{\max} \tag{10}$$

Rearranging terms, we obtain the following inequality:

$$\mathbf{d}(s)\,\dddot{s} + \mathbf{e}(s)\,\dot{s}\ddot{s} + \mathbf{f}(s)\,\dot{s}^3 + \mathbf{g}(s) \le 0, \tag{11}$$

where the coefficients are defined as:

$$\mathbf{d}(s) = \begin{pmatrix}\mathbf{q}'(s)\\ -\mathbf{q}'(s)\end{pmatrix}, \quad \mathbf{e}(s) = \begin{pmatrix}3\mathbf{q}''(s)\\ -3\mathbf{q}''(s)\end{pmatrix},$$
$$\mathbf{f}(s) = \begin{pmatrix}\mathbf{q}'''(s)\\ -\mathbf{q}'''(s)\end{pmatrix}, \quad \mathbf{g}(s) = \begin{pmatrix}-\mathbf{j}_{\max}\\ \mathbf{j}_{\min}\end{pmatrix}.$$

This formulation yields a set of linear constraints on $\dddot{s}$ at each state $(s,\dot{s},\ddot{s})$. For each inequality indexed by i, the admissible jerk range can be computed analytically. Specifically, for entries where $d_i(s) \ne 0$, the inequality can be solved for $\dddot{s}$ as:

- If $d_i(s) > 0$, then $\dddot{s} \le \gamma_i = \frac{-e_i(s)\dot{s}\ddot{s} - f_i(s)\dot{s}^3 - g_i(s)}{d_i(s)}$
- If $d_i(s) < 0$, then $\dddot{s} \ge \eta_i = \frac{-e_i(s)\dot{s}\ddot{s} - f_i(s)\dot{s}^3 - g_i(s)}{d_i(s)}$

Thus, the overall feasible jerk interval at a given state is bounded by the maximum of all lower bounds and the minimum of all upper bounds:

$$\gamma(s,\dot{s},\ddot{s}) = \min_i \gamma_i(s,\dot{s},\ddot{s}), \eta(s,\dot{s},\ddot{s}) = \max_i \eta_i(s,\dot{s},\ddot{s}) \tag{12}$$

A trajectory satisfies the jerk constraints if and only if the path jerk $\dddot{s}$ lies within the range:

$$\eta(s,\dot{s},\ddot{s}) \le \dddot{s} \le \gamma(s,\dot{s},\ddot{s}) \tag{13}$$

C. Challenges in Jerk- and Torque-Constrained Optimal Trajectories

To achieve time-optimal motion along a fixed path under torque constraints, a common approach is to discretize the path and optimize the evolution of the squared velocity $x = \dot{s}^2$ across each segment. Assuming uniform acceleration (or deceleration) between adjacent discretized points, the kinematic relation is expressed as

$$x_{i+1} = x_i + 2\Delta_i u_i, \tag{14}$$

TOPP problem with bounded velocities and Torque is generally formulated as:

max x_i, subject to:

$$\begin{cases} X_{min} \le x_i \le X_{max} \\ \tau_{min} \le a(s)u + b(s)x + c(s) \le \tau_{max} \\ X_{min} \le x_i + 2\Delta_i u_i \le X_{max} \end{cases}$$
$$i = 2, \cdots, N-1 \tag{15}$$

IEEE Transactions on Automation Science and Engineering (T-ASE) paper, presented at ICRA 2026, Vienna, Austria.

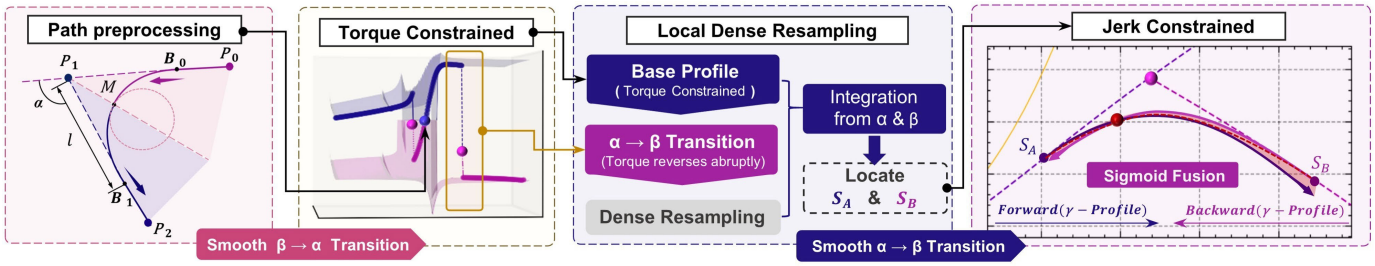

Fig. 2. Overview of the proposed algorithm. The process begins with a torque-constrained TOPP (base profile), identifies torque-switch points where torque reverses abruptly, performs local resampling around these points, applies jerk-limited integration from both sides, and fuses the resulting profiles using sigmoid blending. The final trajectory is continuous in jerk while satisfying all torque constraints.

where x and u are the optimization variables, X_{min} and X_{max} denote the bounds of velocity, τ_{min} and τ_{max} denote the bounds of torque. Iteratively solving the problem according to Eq. (15) involves maximizing the output torque of each segment under constraints, thereby maximizing the path acceleration u to achieve the goal of time-optimal trajectory.

However, while the problem remains convex when only velocity and torque constraints are considered, the introduction of jerk constraints significantly increases its complexity.

Specifically, jerk constraints require bounding the third derivative of the path parameter $s(t)$, elevating the system to third-order dynamics and expanding the trajectory planning state space to include $(s, \dot{s}, \ddot{s})$. Moreover, the interdependence between position, velocity, acceleration, and jerk breaks the convexity of the feasible region. The torque, which depends nonlinearly on these derivatives, further complicates the optimization landscape.

Consequently, time-optimal trajectory planning under simultaneous torque and jerk constraints becomes a non-convex problem, rendering standard convex optimization methods inapplicable.

III. Time-Optimal Planning Under Torque and Jerk Constraints

To further clarify our approach, this section presents the proposed hybrid planning framework. As illustrated in Fig. 2, the process begins with classical torque-constrained TOPP, which generates a baseline trajectory that satisfies all torque limits but may exhibit excessively large jerk. To enhance dynamic feasibility, we detect key switching points characterized by abrupt torque reversals and locally resample the trajectory in their vicinity. Forward and backward jerk-limited integration is then applied to reconstruct these segments, followed by smooth sigmoid blending to fuse them into a unified, continuous trajectory. The resulting trajectory remains time-optimal and torque-feasible while satisfying jerk constraints. The remainder of this section provides a detailed description of each step in the framework.

A. Torque-Feasible Baseline Trajectory Generation

By solving the convex optimization problem of Eq (15), a time-optimal trajectory along a given path subject to torque constraints can be obtained. As illustrated in Fig. 1, the resulting profile adheres to the structure prescribed by Pontryagin's Maximum Principle, where the trajectory alternates between the acceleration-saturated $\alpha(s, \dot{s})$ and deceleration-saturated $\beta(s, \dot{s})$. These bounds are derived from torque feasibility and represent the minimum and maximum permissible accelerations at each point along the path.

Transitions from β to α typically exhibit continuity in acceleration, resulting in relatively smooth motion. The smoothness in such segments is primarily influenced by the geometric and differential properties of the underlying path, especially its curvature and higher-order continuity. In practice, ensuring a sufficiently smooth, $\mathcal{C}^2$-continuous path during preprocessing is critical for enabling high-speed, torque-feasible motion [25].

Conversely, transitions from α to β are characterized by discontinuities in acceleration between adjacent discretization points. These abrupt changes often manifest as instantaneous reversals in joint torque, corresponding to classical Bang-Bang control behavior. While such transitions guarantee strict time optimality, they induce large jerk values, which can significantly impair the dynamic feasibility and physical safety of motion execution on real-world robotic systems. To mitigate these issues, the subsequent section introduces a jerk-limited refinement procedure specifically targeting these high-jerk transition zones, thereby enhancing trajectory smoothness without sacrificing overall time efficiency.

B. Jerk-Bounded Refinement via Bidirectional Resampling and Integration

In the context of trajectory optimization under third-order constraints, Pontryagin's Maximum Principle dictates that time-optimal motion must transition between maximum and minimum jerk segments in a structured sequence. When both torque and jerk constraints are imposed, the resulting hybrid trajectory must satisfy a series of coordinated switching events that blend torque-limited and jerk-limited dynamics. Specifically, four key transitions are identified [13], [18]:

- **Torque-limited to maximum jerk phase:** $\alpha \to \gamma$, where the trajectory departs from the torque-constrained envelope and enters the jerk-constrained integration phase, initiating a smooth transition beyond abrupt torque reversals.
- **Maximum to minimum jerk phase:** $\gamma \to \eta$, representing the internal jerk inversion necessary for smooth motion. This phase often arises due to the difficulty of realizing an exact $\alpha \to \gamma \to \beta$ sequence, and η serves as

IEEE Transactions on Automation Science and Engineering (T-ASE) paper, presented at ICRA 2026, Vienna, Austria.

an intermediate blending point to ensure continuity and feasibility.

- **Minimum to maximum jerk phase:** $\eta \rightarrow \gamma$, re-accelerating with bounded jerk to align with the trajectory's continuation and maintain consistency with both dynamic limits and the time-optimal goal.
- **Maximum jerk to minimum torque phase:** $\gamma \rightarrow \beta$, marking the terminal transition from jerk-constrained integration back to the torque-limited regime, thereby completing the hybrid trajectory structure with both torque feasibility and jerk continuity.

1) Dense Sampling of the Base Profile: To refine the trajectory segments subject to jerk constraints, we first locate each $\alpha \rightarrow \beta$ switching region on the torque-constrained baseline profile. Around each identified switching point, a non-symmetric resampling window $[t_{\text{sw}} - \Delta t_1,\, t_{\text{sw}} + \Delta t_2]$ is defined to cover the dynamically active range between the two adjacent valleys surrounding the switching point. The window lengths Δt_1 and Δt_2 are automatically computed as the time intervals between t_{sw} and the nearest preceding and following local minima of the velocity profile, thereby ensuring complete coverage of the transition region without unnecessarily extending the integration range.

Within this window, the trajectory segment is uniformly resampled in time, where t_{sw} denotes the estimated $\alpha \rightarrow \beta$ switching instant. The resampled segment consists of N points with a fixed time step δt. The integration step δt is a user–configurable parameter that determines both the numerical accuracy and the computational cost of the subsequent jerk-constrained integration, expressed as:

$$\left\{(s_j,\, \dot{s}_j,\, \ddot{s}_j,\, \delta t)\right\}_{j=0}^{N}. \tag{16}$$

These high-resolution anchor points not only enable precise localization of optimal torque-to-jerk transition points (e.g., $\alpha \rightarrow \gamma$, $\gamma \rightarrow \beta$), but also provide the temporal discretization necessary for constructing jerk-constrained segments through bidirectional integration.

2) Bidirectional Integration Under Jerk Constraints: After extracting the dense sampling points $\{(s_j, \dot{s}_j, \ddot{s}_j)\}$ from the α segment of the base trajectory, the objective of this subsection is to accurately localize the optimal torque-to-jerk transition points, i.e., $\alpha \rightarrow \gamma$ and $\gamma \rightarrow \beta$. This is achieved via bidirectional numerical integration under bounded jerk constraints.

a) Forward integration from α: For each sampling point $\{(s_j, \dot{s}_j, \ddot{s}_j)\}$ on the α-profile, we perform forward integration under a prescribed jerk profile $\gamma(s, \dot{s}, \ddot{s})$. During each step, the path coordinate s_j remains fixed, while the velocity and acceleration are updated using:

$$\delta t_j = \frac{(s_{j+1} - s_j)}{\dot{s}_j}, \tag{17}$$

$$\ddot{s}_{j+1} = \ddot{s}_j + \gamma(s_j, \dot{s}_j, \ddot{s}_j) \cdot \delta t_j, \quad \dot{s}_{j+1} = \dot{s}_j + \ddot{s}_j \cdot \delta t_j. \tag{18}$$

This forward integration yields a trajectory denoted by:

$$\mathcal{P}(\gamma, S_{\text{start}}), \tag{19}$$

where $S_{\text{start}} = (s_{\text{start}}, \dot{s}_{\text{start}}, \ddot{s}_{\text{start}})$ is the initial integration point.

To identify the optimal $\alpha \rightarrow \gamma$ switching point, we employ a bisection-based shooting search that locates the last forward-integrated γ-profile that stays outside the β-envelope:

$$\{\mathcal{P}(\gamma, S_k)\} \cap \beta = \emptyset, \quad \left\{\mathcal{P}(\gamma, S_{k+1})\right\} \cap \beta \neq \emptyset. \tag{20}$$

As illustrated in Fig. 3 (A), this corresponds to identifying the forward-integrated γ-profile that remains outside the β boundary, while the subsequent profile enters the deceleration region defined by β. Therefore, the point S_A is selected as the optimal transition point for initiating the jerk-limited segment.

b) Backward integration from β: A symmetric procedure is used to determine the $\gamma \rightarrow \beta$ transition point. Starting from dense samples on the β-profile, backward integration is carried out under the same jerk bound, now with decreasing s. The optimal switching point S_B is obtained as the last backward-integrated γ-profile that remains entirely outside the α-envelope before intersecting it at the previous sampling index.

c) Uniqueness and convergence: Because the torque-based TOPP profile defines, at every resampled point around an $\alpha \rightarrow \gamma$ transition, a non-empty convex acceleration interval $[\alpha(s_j), \beta(s_j)]$, both the forward and backward shooting trajectories evolve within this feasible region under bounded jerk until they first intersect the opposite boundary. Over the densely sampled window surrounding each switching region, the Boolean indicator that marks whether a shooting trajectory intersects the target boundary exhibits a monotonic pattern along the ordered samples. Therefore, a unique transition index exists at which this indicator switches value, and the proposed bisection method converges to this index in logarithmic time.

Algorithm 1 Bisection-Based Bidirectional Shooting

Input: Dense path samples $\{S_j = (s_j, \dot{s}_j, \ddot{s}_j)\}_{j=0}^{N}$; jerk bound $\gamma(s, \dot{s}, \ddot{s})$
Output: Transition points S_A, S_B and jerk-limited trajectories $\mathcal{P}_A$, $\mathcal{P}_B$
Procedure BISECTIONSHOOT(direction):
  $L \leftarrow 0$, $R \leftarrow N$
while $R - L > 1$ **do**
    $M \leftarrow \lfloor (L + R)/2 \rfloor$
    $\mathcal{P} \leftarrow$ integrate trajectory from S_M in given direction under jerk limit $\gamma(s, \dot{s}, \ddot{s})$
  if trajectory intersects the opposite boundary **then**
    $R \leftarrow M$
  else
    $L \leftarrow M$
  end if
end while
  return $(S_R, \mathcal{P})$
$(S_A, \mathcal{P}_A) \leftarrow$ BISECTIONSHOOT(`forward from` α)
$(S_B, \mathcal{P}_B) \leftarrow$ BISECTIONSHOOT(`backward from` β)
Return: S_A, S_B, $\mathcal{P}_A$, $\mathcal{P}_B$

The overall procedure for identifying the torque-to-jerk transition points via forward and backward integration is summarized in Algorithm 1.

IEEE Transactions on Automation Science and Engineering (T-ASE) paper, presented at ICRA 2026, Vienna, Austria.

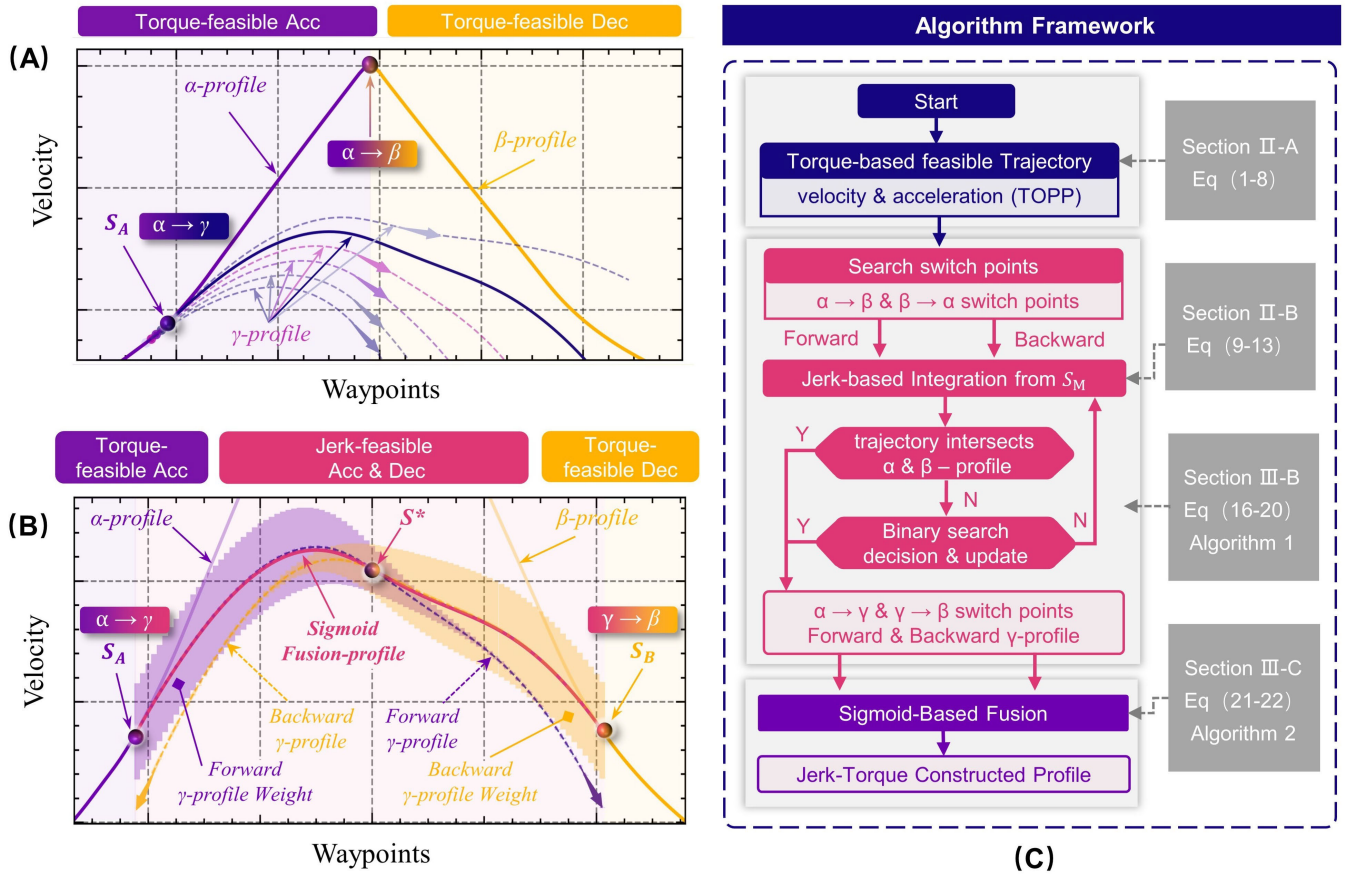

Fig. 3. **Overall framework of the proposed jerk–torque–constrained trajectory planning method.** (A) Shooting-based identification of the $\alpha \rightarrow \gamma$ transition point. Among multiple forward-integrated γ-profiles from the α-profile, the one starting at S_A is the last that remains outside the β -profile. Its successor intersects β, indicating S_A as the closest feasible switching point. (B) Bidirectional integration of jerk-feasible profiles and sigmoid-based fusion between the forward and backward γ-trajectories to construct a continuous jerk-limited transition ($S_A \rightarrow S_B$). (C) Algorithmic framework showing the complete workflow of the proposed method. Section references correspond to the detailed formulations and algorithms described in the text.

C. Sigmoid-Based Fusion of Forward and Backward Profiles

Due to the inherent instability of third-order derivatives under dense interpolation, the original interpolation scheme encounters severe numerical challenges as the sampling interval decreases. In particular, dense resampling tends to amplify minor numerical discontinuities in acceleration, leading to uncontrolled jerk magnitudes and a breakdown in numerical convergence. Consequently, the trajectory transition—spanning from α-profile through the intermediate γ-profile to β-profile—becomes ill-conditioned and increasingly difficult to constrain.

A traditional remedy is to introduce a short reverse–jerk segment—often interpreted as an η-profile—to locally correct the discontinuity and restore feasibility near the connection point [18]. However, as noted by the authors, constructing such a reverse segment requires solving an additional boundary value problem (BVP) on top of the original jerk-integration procedure. This nested BVP substantially increases computational complexity, and the resulting auxiliary segment does not correspond to the natural structure of the optimal solution, thereby introducing unnecessary redundancy into the trajectory.

To address these limitations, we propose a closed-form fusion method based on a sigmoid weighting function. Noting that the forward and backward velocity profiles retain local smoothness under dense sampling, their pointwise deviation remains bounded. Therefore, a convex combination can be applied to smoothly blend them, avoiding explicit η construction while suppressing jerk discontinuities near the transition boundary.

To construct the fused trajectory, we denote the forward-integrated and backward-integrated jerk-limited velocity profiles as $\mathcal{P}(\gamma, S_A)$ and $\mathcal{P}(\gamma, S_B)$, respectively. A smooth transition is achieved by defining a sigmoid weight function $w(s)$ centered at the intersection point S^*, where $v_{\text{fwd}}(S^*) = v_{\text{bwd}}(S^*)$. The fused velocity profile is then computed as:

$$v_{\text{fused}}(s) = w(s)\, v_{\text{fwd}}(s) + [1 - w(s)]\; v_{\text{bwd}}(s), \tag{21}$$

where $w(s)$ takes the logistic form:

$$w(s) = \frac{1}{1 + e^{\alpha(s - S^*)}}, \tag{22}$$

The parameter $\alpha > 0$ controls the steepness of the transition. When selected relative to the fusion-window length, the logistic weight becomes effectively saturated near the interval boundaries, yielding $w(s) \approx 1$ around S_A and $w(s) \approx 0$ near S_B, thereby producing a smooth S-shaped blending rather than a hard switch.

As illustrated in Fig. 3(B), the shaded weight bands show how the contributions of the forward and backward profiles

IEEE Transactions on Automation Science and Engineering (T-ASE) paper, presented at ICRA 2026, Vienna, Austria.

TABLE I
JOINT TORQUE LIMITS USED IN EXPERIMENTS (UNIT: NM)

JOINT INDEX	1	2	3	4	5	6
MIN TORQUE	−120	−120	−120	−42	−42	−20
MAX TORQUE	120	120	120	42	42	20

vary gradually across the interval. By centering the sigmoid within the fusion window and letting the weight saturate smoothly near S_A and S_B, the fused velocity naturally aligns with the forward profile at the entrance, with the backward profile at the exit, and transitions smoothly between them within the interior. This eliminates the slope mismatches that would otherwise occur at the $\alpha-\gamma-\beta$ junctions and removes the primary sources of acceleration or jerk discontinuity.

From a theoretical standpoint, both $v_{\text{fwd}}(s)$ and $v_{\text{bwd}}(s)$ are generated by integrating bounded jerk and are therefore at least C^1 functions of the path coordinate s. Since the logistic weight $w(s)$ is C^∞, the fused profile defined in (21) inherits differentiability from its components. In practice, selecting the steepness parameter α relative to the fusion-window length ensures weight saturation at the boundaries and a smooth interior transition, yielding a fused velocity with a continuous first derivative across the entire segment. After the time reparameterization $dt/ds = 1/\dot{s}(s)$, the resulting acceleration $\ddot{s}(t)$ remains continuous and the jerk $\dddot{s}(t)$ stays bounded, producing a trajectory that is effectively C^2 over the complete $\alpha-\gamma-\beta$ transition.

Algorithm 2 Sigmoid Fusion of Forward and Backward Velocity Profiles

1: **Input:** Forward profile $v_{\text{fwd}}(s)$, backward profile $v_{\text{bwd}}(s)$, path coordinates $\mathcal{S}$
2: **Output:** Fused smooth profile $v_{\text{fused}}(s)$
3: Find intersection point S^* where $v_{\text{fwd}}(S^*) = v_{\text{bwd}}(S^*)$
4: **for** $s \in \mathcal{S}$ **do**
5: Calculate sigmoid weight $w(s)$ (Eq. (22))
6: Compute fused velocity $v_{\text{fused}}(s)$ (Eq. (21))
7: **end for**
8: **Return:** $v_{\text{fused}}(s)$

Compared with velocity-scaling or optimization-based approaches, the proposed sigmoid fusion provides a low-complexity yet dynamically feasible refinement mechanism. The logistic weighting acts as a numerical low-pass filter that suppresses high-frequency artifacts introduced by discretization, while the feasibility of $v_{\text{fwd}}(s)$ and $v_{\text{bwd}}(s)$ ensures that the fused trajectory automatically satisfies velocity, acceleration, and jerk constraints without requiring post-smoothing or switching-point tuning. The complete procedure is summarized in Algorithm 2.

IV. EXPERIMENTAL EVALUATION

To validate the effectiveness of the proposed hybrid time-optimal trajectory planning framework under torque and jerk constraints, two representative experiments were conducted on a Siasun T12A industrial robot.

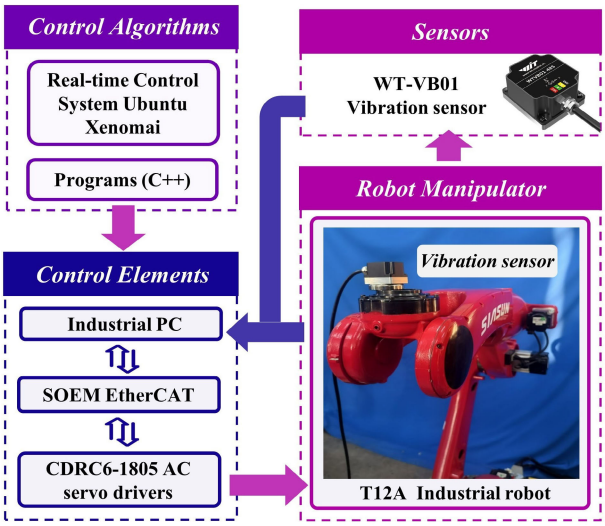

Fig. 4. Real-time experimental platform for a six-axis industrial robot with EtherCAT control and vibration sensing.

The experimental platform is shown in Fig. 4. The robot runs real-time control algorithms on an Ubuntu system equipped with the Xenomai real-time kernel and the Simple Open EtherCAT Master (SOEM). The control hardware includes an industrial PC and CoolDrive RC6-1805 AC servo drivers connected via the EtherCAT bus. For real-time motion feedback, the robot is equipped with a WT-VB01 vibration sensor. A servo control cycle of 1 ms was employed to ensure high-frequency, low-latency control based on the real-time EtherCAT communication architecture. The torque limits applied to each joint are listed in Table I.

Throughout the experiments, we simultaneously recorded the rate of change in joint torque feedback across all joints and the three-axis vibration signals at the end-effector. These data were employed to quantitatively evaluate motion stability and execution precision. The experimental scenarios encompass both a representative high-speed motion task and a complex planar trajectory tracking task, aiming to comprehensively assess the feasibility and robustness of the proposed method under varied dynamic constraints.

To ensure a rigorous evaluation, we conducted a comprehensive comparison against both a torque-constrained baseline based on TOPP-RA [13] and a representative jerk-constrained method [23]. Relative to TOPP-RA, the proposed hybrid time-optimal planning framework markedly reduces joint-torque fluctuations and end-effector vibrations while maintaining comparable computational cost, thereby improving actuator dynamic stability and overall motion smoothness. Compared with the jerk-limited algorithm of [23], our method imposes the jerk bounds directly in joint space, enabling more aggressive yet feasible trajectory execution and resulting in consistently smoother joint profiles, even along highly curved or dynamically demanding segments.

As shown in Fig. 5, the algorithm runtime increases almost linearly with the number of interpolation points, confirming the scalability and computational efficiency of the proposed planner under high-resolution trajectory settings. Compared

IEEE Transactions on Automation Science and Engineering (T-ASE) paper, presented at ICRA 2026, Vienna, Austria.

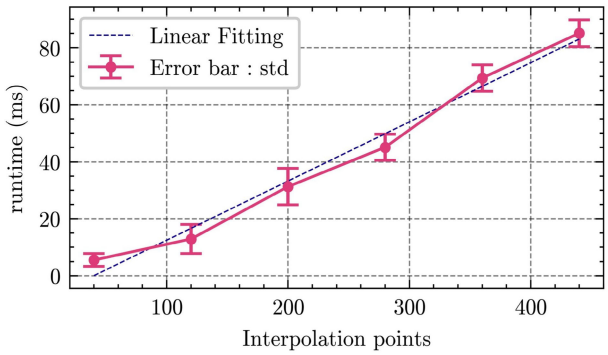

Fig. 5. Relationship between the additional computation time introduced by jerk constraints (on top of torque-limited TOPP-RA) and the number of interpolation points.

TABLE II
COMPUTATION TIME OF DIFFERENT METHODS WITH 500 DISCRETIZATION POINTS

	TOPP-RA [13]	CO Method [23]	Ours
Runtime (ms)	486.4	908.7	609.5

with the TOPP-RA algorithm, the total computation time of our method slightly increases due to the additional *bidirectional shooting* and *trajectory fusion* procedures applied near switching points. Nevertheless, the inclusion of jerk constraints markedly enhances the suppression of acceleration discontinuities and improves overall trajectory smoothness.

In terms of complexity, each shooting iteration requires a short integration over a local resampling window around the switching point. Since the number of such windows is limited and their total length grows proportionally with the global discretization size, the overall computational overhead introduced by the shooting process also scales approximately linearly with N. Therefore, the proposed planner maintains an effective $\mathcal{O}(N)$ runtime behavior, consistent with the empirical trend observed in Fig. 5.

As summarized in Table II, when the number of interpolation points is set to 500, the computation time increases by only about 100 ms (approximately 20% higher than TOPP-RA), while the proposed method remains considerably faster than optimization-based frameworks such as [23].

A. Performance Assessment on Complex Trajectories With Dynamic Constraints

To rigorously evaluate the proposed hybrid planning framework under realistic dynamic constraints, a challenging test trajectory was constructed featuring multiple curvature variations and direction reversals, as illustrated in Fig. 6. The trajectory was pre-smoothed using the method in [25] to avoid numerical singularities while preserving regions of high dynamic demand. These characteristics induce substantial fluctuations in joint torques and necessitate frequent acceleration–deceleration transitions, making the trajectory particularly suitable for benchmarking jerk-limited planning algorithms.

In this experiment, all planners were evaluated under the identical joint torque limits summarized in Table I. The proposed method additionally imposes a uniform joint-space jerk bound of 250 rad/s^3 on each joint. For the convex-optimization-based method in [23], where jerk constraints are formulated in Cartesian space, the end-effector jerk bound was set to 120 m/s^3 after empirical calibration to ensure both feasibility and numerical stability.

Figures 7 and 8 present the simulated Cartesian motion profiles and the corresponding joint-level torque and jerk distributions. As shown in Fig. 8(A), the bang–bang structure of TOPP-RA results in pronounced jerk spikes and abrupt torque transitions, which can increase mechanical stress and degrade motion smoothness. Both our method and the convex-optimization-based approach in [23] mitigate such discontinuities by explicitly incorporating higher-order dynamic constraints into the planning process.

However, when examining the joint-acceleration profiles in Fig. 8(B), a fundamental limitation of [23] becomes apparent. Because its jerk constraints are enforced in Cartesian space, the resulting smoothness cannot be consistently propagated through the Jacobian mapping, especially in regions where the Jacobian varies rapidly. As highlighted by the red circles in Fig. 8(B), some joints exhibit pronounced spikes in jerk—reaching nearly twice the magnitude observed in smoother segments—while in other portions of the trajectory, the available jerk capacity remains significantly underutilized. This mismatch indicates that Cartesian-space jerk constraints cannot fully guarantee joint-level dynamic feasibility and therefore cannot achieve true time optimality under coupled joint-acceleration and joint-jerk limits.

In contrast, the trajectory generated by the proposed method (Fig. 8(C)) exhibits a well-structured alternation between *torque-saturated* and *jerk-saturated* phases. The planner explicitly transitions through torque-limited acceleration, jerk-limited switching, and torque-limited deceleration. This coordinated activation of constraints enables the method to balance time efficiency and motion smoothness while ensuring that all actuator limits are strictly satisfied.

Because the proposed method is more robust in regions with rapidly changing Jacobians and better utilizes the joint-space jerk limits elsewhere, it can achieve higher feasible velocities along the path. This also explains why, in Fig. 7, our method is faster than the CO method [23] in most segments, but slightly slower in a few others.

Fig. 9 shows the experimentally measured joint torque-rate profiles obtained during the execution of trajectories generated by TOPP-RA, the CO method [23], and the proposed approach. The shaded areas highlight two distinct motion phases. In the execution phase (blue shaded region), the proposed method achieves substantially smoother joint actuation, indicating superior compliance and reduced dynamic stress. In the motion-termination phase (pink shaded region), TOPP-RA exhibits pronounced residual oscillations caused by abrupt changes in acceleration, whereas the proposed method significantly suppresses these vibrations, resulting in faster settling behavior and improved end-effector stability.

Table III summarizes the root-mean-square (RMS) torque-rate values for all joints, as well as the integrated squared torque rate (ISTR) over the entire path. Both the CO method

IEEE Transactions on Automation Science and Engineering (T-ASE) paper, presented at ICRA 2026, Vienna, Austria.

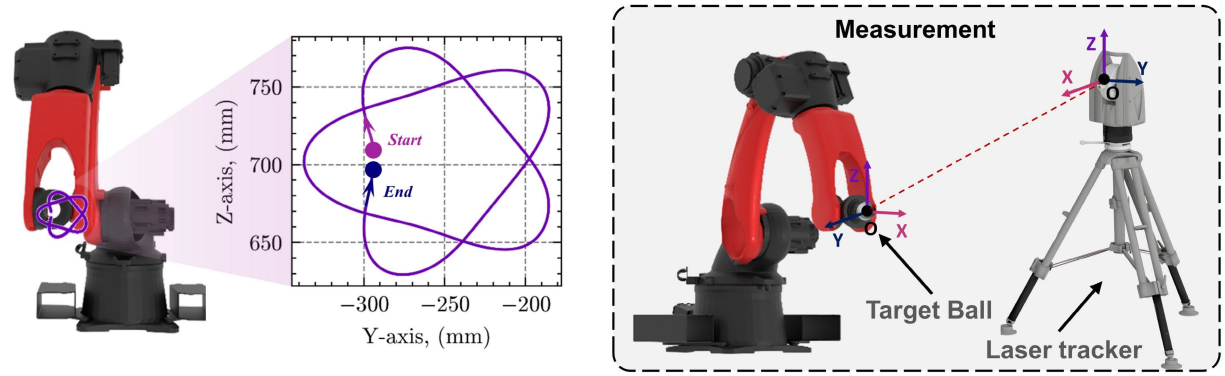

Fig. 6. The experimental setup includes the visualization of the test trajectory and a smoothness evaluation platform. The purple curve represents the spatial path executed by the robot end-effector, with the inset showing its projection onto the YZ plane. During the experiment, a laser tracker was used to monitor the final vibration stability of the motion trajectory.

TABLE III
RMS TORQUE-RATE (NM/S) AND ISTR ($\int \dot{\tau}^2 dt$) WITH REDUCTION RATIOS RELATIVE TO TOPP-RA

(A) RMS torque-rate (Nm/s) with reduction ratios (↓%)						
Method	J1	J2	J3	J4	J5	J6
TOPP-RA	4140	4110	1080	432	148	83.7
CO Method [23]	2390 (42.4%)	2280 (44.6%)	617 (43.2%)	283 (34.5%)	135 (8.58%)	75.9 (9.32%)
Ours	**1830 (55.8%)**	2330 (43.5%)	628 (42.1%)	270 (37.6%)	135 (8.56%)	71.4 (14.8%)
(B) ISTR ($\int \dot{\tau}^2 dt$) with reduction ratios (↓%)						
Method	J1	J2	J3	J4	J5	J6
TOPP-RA	9.71×10^7	9.59×10^7	6.67×10^6	1.06×10^6	1.24×10^5	3.96×10^4
CO Method [23]	3.28×10^7 (66.3%)	2.98×10^7 (68.9%)	2.18×10^6 (67.3%)	4.60×10^5 (56.4%)	1.05×10^5 (15.3%)	3.31×10^4 (16.6%)
Ours	$\mathbf{1.92\times10^7}$ **(80.2%)**	3.09×10^7 (67.8%)	2.24×10^6 (64.9%)	4.16×10^5 (66.4%)	1.05×10^5 (15.5%)	2.91×10^4 (26.6%)

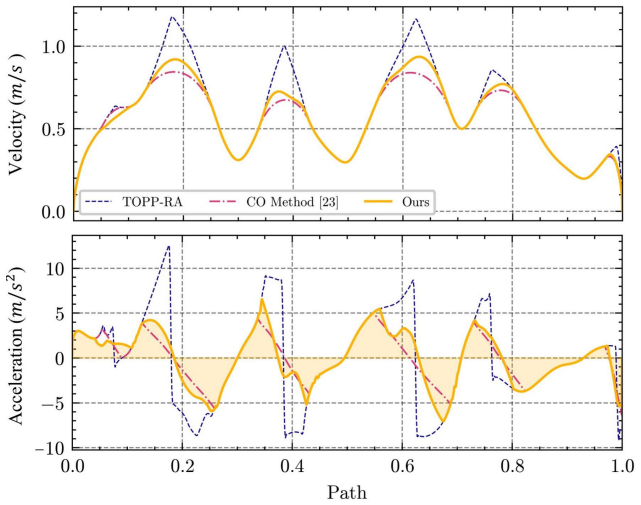

Fig. 7. Planned end-effector velocity and acceleration profiles generated by different trajectory planning algorithms under identical torque and path constraints.

[23] and the proposed approach yield substantially smoother torque transitions than TOPP-RA, leading to markedly reduced torque-rate magnitudes and mitigating abrupt changes that may excite structural resonances or accelerate wear in the actuators and transmission components. This advantage is particularly critical for systems with limited structural stiffness, where elastic vibrations are more easily amplified.

TABLE IV
RMS VIBRATION METRICS AND REDUCTION RATIOS RELATIVE TO TOPP-RA IN X, Y, AND Z DIRECTIONS

Metric	**TOPP-RA (RMS)**	**CO Method [23] (RMS / ↓%)**	**Ours (RMS / ↓%)**
Y-direction			
Time RMS (g)	0.341	0.227 / 33.4	**0.206 / 39.8**
PSD RMS (g^2/Hz)	0.161	0.098 / 39.1	**0.084 / 47.8**
Z-direction			
Time RMS (g)	0.377	0.180 / 52.2	**0.175 / 53.7**
PSD RMS (g^2/Hz)	0.181	0.0827 / 54.3	**0.0775 / 57.2**
X-direction			
Time RMS (g)	0.138	0.0530 / 61.5	0.0568 / 58.7
PSD RMS (g^2/Hz)	0.102	0.0416 / 59.2	0.0423 / 58.5

Moreover, the results show that the CO method and the proposed approach achieve nearly identical torque-rate performance on Joints 2–6, while on Joint 1 our method attains a notably lower torque-rate. This observation aligns with the red-circled region in Fig. 9 (Joint 1) and is consistent with the simulation trends in Fig. 8. The agreement between experimental and simulation results reinforces that the proposed method provides superior joint-torque stability, especially in regions where the Jacobian varies rapidly.

Fig. 10 presents the three-axis vibration accelerations measured at the end-effector during trajectory execution for

IEEE Transactions on Automation Science and Engineering (T-ASE) paper, presented at ICRA 2026, Vienna, Austria.

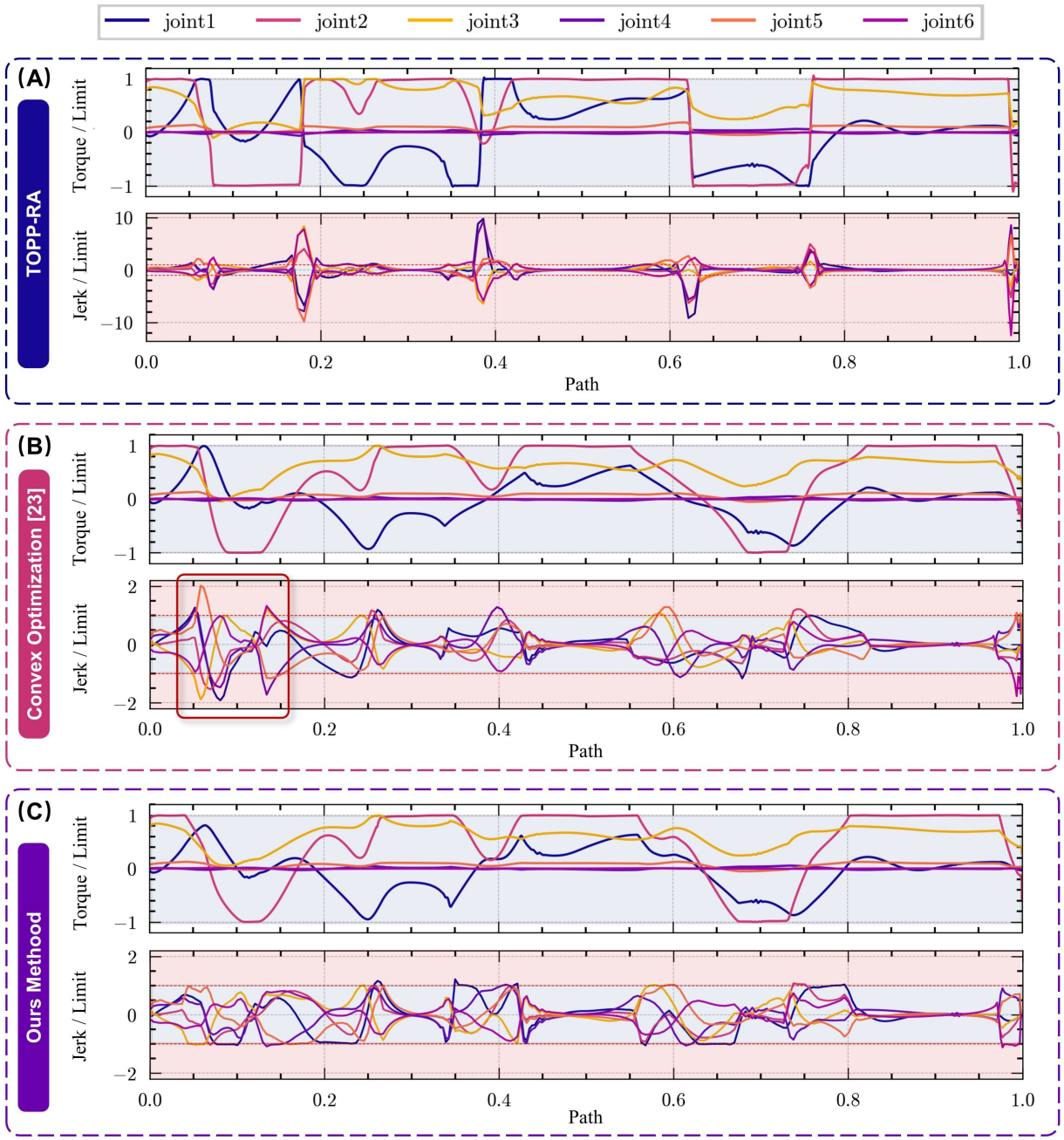

Fig. 8. Comparison of normalized joint torque and jerk profiles obtained using different trajectory planning algorithms under identical torque limits. (a) TOPP-RA, (b) convex-optimization-based method [23], and (c) the proposed method.

TOPP-RA, the CO method, and the proposed approach. Since the end-effector motion is primarily confined to the Y-Z plane, the vibrations are predominantly observed along the Y and Z axes. Table IV summarizes the quantitative metrics, including the RMS values along the X, Y, and Z axes, as well as the RMS values based on power spectral density (PSD). It is evident that TOPP-RA exhibits relatively high vibration amplitudes across all axes, while both the CO method [23] and the proposed approach effectively suppress oscillations in both time and frequency domains. Notably, the time-domain RMS values and PSD RMS values are significantly reduced, indicating a substantial attenuation of high-frequency energy input into the system. These results highlight the theoretical efficacy of imposing jerk constraints to limit high-frequency excitation and mitigate vibration propagation in the serial manipulator structure.

Compared to the CO method [23], our approach also demonstrates better stability at the end-effector, particularly in the Y-axis data in Table IV and the red-circled region in Fig. 10. The vibration reduction achieved by our method in this region is consistent with the results shown in the red-circled regions of Figs. 9 and 8, further demonstrating that our algorithm exhibits superior robustness in regions where the Jacobian matrix undergoes rapid changes.

Figure 11 shows the end-effector displacement measured along the Y and Z axes using a laser tracker under identical

IEEE Transactions on Automation Science and Engineering (T-ASE) paper, presented at ICRA 2026, Vienna, Austria.

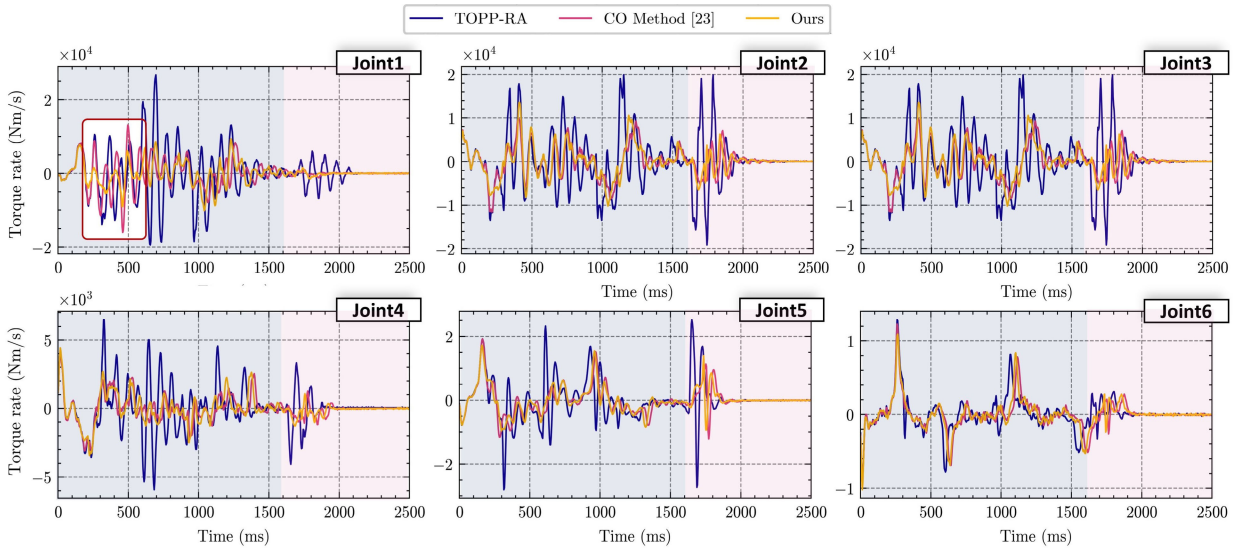

Fig. 9. Joint torque rate curves during trajectory execution. The front portion (blue background) corresponds to the execution phase, while the back portion (pink background) corresponds to the residual vibration.

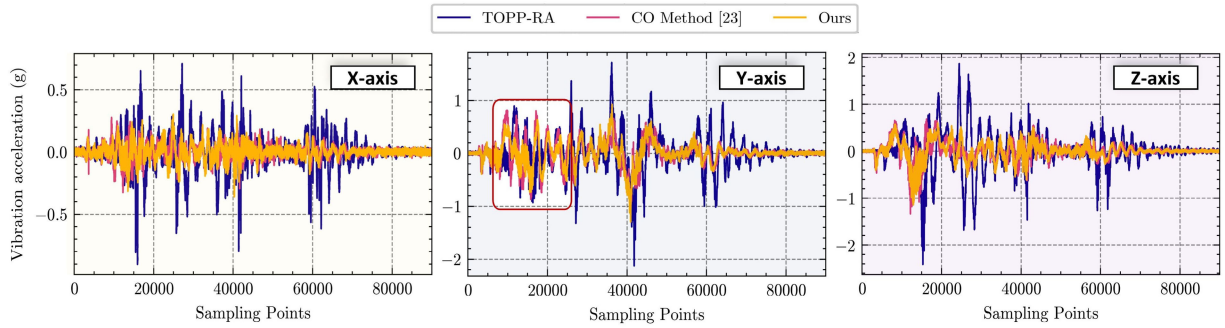

Fig. 10. Comparison of vibration data collected from the end-effector's 3D vibration sensor under identical torque constraints using different algorithms.

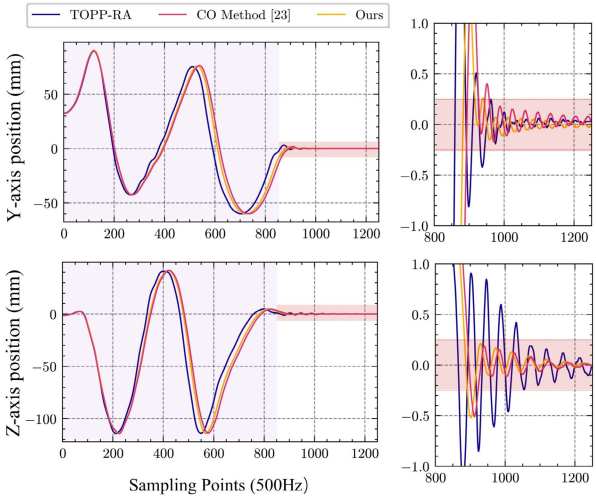

Fig. 11. Comparative analysis of end-effector displacement measured by a laser tracker under identical torque constraints using different trajectory planning algorithms, highlighting the determination of motion settling time.

torque constraints for the three trajectory planning methods. The red-shaded region highlights the post-motion attenuation phase, during which residual vibrations dominate the stabilization behavior. The settling time is defined as the duration

TABLE V
EXECUTION TIME METRICS AND REDUCTION RATIOS RELATIVE TO TOPP-RA

Metric	TOPP-RA (Value)	CO Method [23] (Value / ↓%)	Ours (Value / ↓%)
Planning Time (ms)	1680	1756 / −4.52	1740 / −3.57
Settling Time (ms)	**2110**	**1914 / 9.29**	**1842 / 12.70**
Jerk Constraint	Not considered	Enforced	Enforced

required for the end-effector trajectory to enter and remain within the ±0.5 mm band, indicating the completion of the stabilization process.

As illustrated in the zoomed-in views on the right of Fig. 11, the TOPP-RA method exhibits pronounced oscillations in both directions, resulting in a noticeably longer settling interval. The CO method reduces the oscillation amplitude relative to TOPP-RA but still presents visible residual vibrations, particularly along the Y axis. In contrast, the proposed method substantially suppresses residual motion, enabling the end-effector trajectory to enter and remain within the ±0.5 mm range significantly earlier.

As summarized in Table V, although TOPP-RA yields the shortest planning time (1680 ms), it produces pronounced pre-settling oscillations in both axes. These oscillations signif-

IEEE Transactions on Automation Science and Engineering (T-ASE) paper, presented at ICRA 2026, Vienna, Austria.

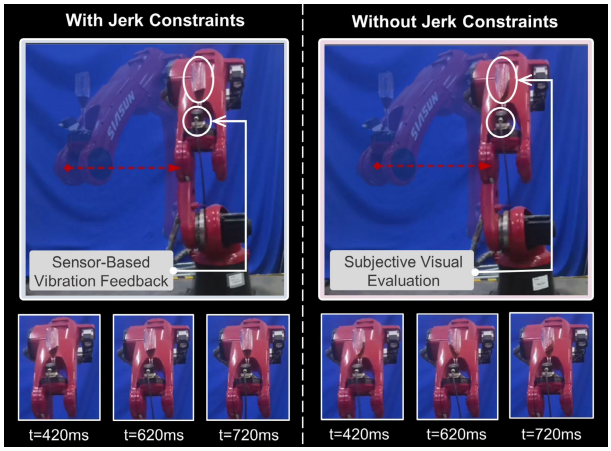

Fig. 12. Liquid-transport experiment comparing different trajectory planners. A cup partially filled with liquid is carried along the prescribed path, where the liquid-surface motion serves as a visual indicator of vibration. The figure highlights differences in sloshing and residual oscillation, with a video provided in the supplementary materials.

icantly prolong the stabilization process, leading to the longest settling time (2110 ms) among all methods. CO method takes the longest planning time (1756 ms), as it conservatively exploits the available acceleration and jerk bounds during optimization. Nevertheless, its explicit jerk constraint produces a noticeable reduction in residual vibrations compared with TOPP-RA, resulting in a shorter settling time (1914 ms). In contrast, the proposed method achieves a more favorable balance between computational efficiency and dynamic smoothness. It provides a competitive planning time (1740ms) while achieving the shortest stabilization time (1842 ms).

B. Dynamic Performance Evaluation on a Straight-Line Transport Task

To further evaluate the dynamic performance of the proposed algorithm during high-speed execution along a fixed Cartesian path, a straight-line liquid-transport experiment was conducted, as shown in Fig. 11. The motion was executed under the torque limits listed in Table I. The evaluation combines quantitative measurements from a 3D vibration sensor mounted on the end-effector with visual inspection of liquid-surface stability, which serves as a sensitive indicator of vibration. Compared with TOPP-RA, which does not enforce jerk constraints, the proposed method generates noticeably smoother motion profiles, maintaining continuous velocity transitions with minimal residual oscillation even when operating near torque saturation.

As illustrated in the supplementary video, the TOPP-RA trajectory induces visible shaking and repeated overshoot during fast motion, exciting the inherent flexibility of the robot links, whereas the proposed jerk-constrained trajectory yields much smoother behavior with a substantially smaller link-deflection response at corresponding time instants. This qualitative observation is corroborated by the sensor-based vibration measurements in Fig. 13. Across all three axes, TOPP-RA exhibits pronounced acceleration bursts—particularly along the Y-axis, the primary direction of motion—originating from abrupt acceleration changes that inject high-frequency excitation into

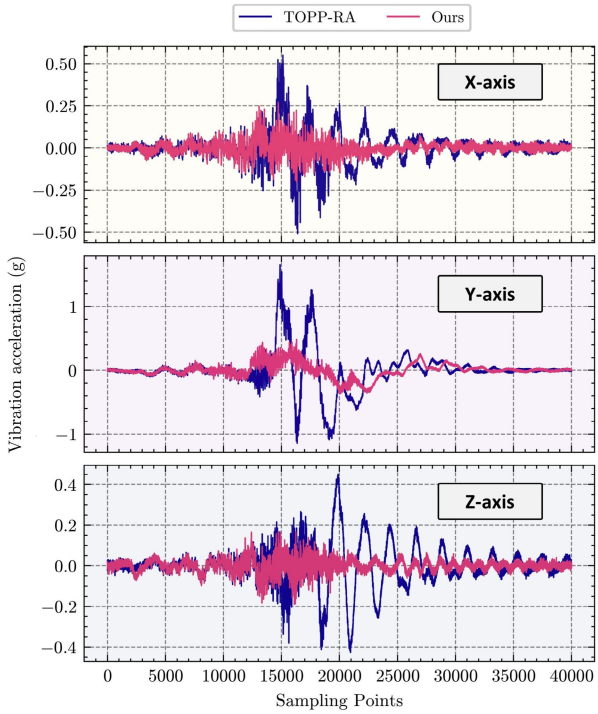

Fig. 13. Comparison of vibration data collected from the end-effector's 3D vibration sensor under identical torque constraints using different algorithms.

TABLE VI
TIME-DOMAIN AND PSD-BASED VIBRATION METRICS FOR TOPP-RA AND OURS (PEAK REMOVED)

Axis	Method	RMS (g)	PSD RMS (g^2/Hz)	Reduction (%)
X	TOPP-RA	0.0646	0.0419	—
	Ours	0.0268	0.0247	58.5 / 41.0
Y	TOPP-RA	0.2175	0.0890	—
	Ours	0.0709	0.0295	67.4 / 66.9
Z	TOPP-RA	0.0715	0.0387	—
	Ours	0.0203	0.0176	71.6 / 54.5

the structure. The proposed method effectively suppresses these high-frequency components, resulting in markedly lower vibration amplitude and faster attenuation of residual oscillation. Quantitative metrics in Table VI further confirm this trend: RMS and PSD-RMS vibration levels are reduced by 58.5%/41.0% on the X-axis, 67.4%/66.9% on the Y-axis, and 71.6%/54.5% on the Z-axis. These consistent reductions across all axes demonstrate that enforcing jerk limits not only smooths local acceleration transitions but also significantly limits the excitation and transmission of structural vibration through the manipulator chain, leading to more stable and dynamically reliable high-speed execution.

V. CONCLUSION

This paper presented a hybrid trajectory planning framework capable of generating time-optimal motion along a fixed end-effector path under joint torque and jerk constraints. The algorithm first constructs a torque-limited trajectory, followed by temporal resampling and a shooting-based procedure to

IEEE Transactions on Automation Science and Engineering (T-ASE) paper, presented at ICRA 2026, Vienna, Austria.

identify the switching points between torque- and jerk-limited phases. By smoothly blending the forward and backward integrated profiles using Sigmoid functions, a globally optimized and dynamically feasible time-parameterized trajectory is obtained.

The proposed method was rigorously validated on a six-degree-of-freedom industrial manipulator equipped with a real-time EtherCAT control system and vibration sensors. Residual vibrations were measured using a laser tracker to determine the settling time, demonstrating the practical applicability and scalability of the approach. Compared with the baseline, the proposed method substantially reduces joint torque fluctuations and end-effector vibrations while preserving near–time-optimal execution time.

To enhance real-world applicability, future work will incorporate more detailed actuator-level dynamics. Examples include nonlinear friction and drivetrain elasticity. Another key direction is to reduce the reliance on precisely known dynamic limits. We aim to introduce adaptive or data-driven estimation of feasible torque, acceleration, and jerk bounds. Such mechanisms can update the dynamic limits online as operating conditions vary. These extensions will improve robustness under modeling uncertainties, payload changes, and unstructured environments. They will also support reliable deployment of the proposed framework in high-speed industrial applications.

REFERENCES

[1] K. Erwinski, A. Wawrzak, and M. Paprocki, "Real-time jerk limited feedrate profiling and interpolation for linear motor multiaxis machines using NURBS toolpaths," *IEEE Trans. Ind. Informat.*, vol. 18, no. 11, pp. 7560–7571, Nov. 2022.

[2] M. Chen, Y. Sun, J. Xu, and J. Liu, "Snap-bounded and time-optimal feedrate scheduling for robotic milling of complex surface parts with analytical solution," *IEEE Trans. Ind. Informat.*, vol. 21, no. 5, pp. 3880–3889, May 2025.

[3] Y. Guo, W. Niu, J. Zhou, and H. Liu, "Near-time optimal feedrate planning for the NURBS curve considering interpolation error constraints," *Robot. Computer-Integrated Manuf.*, vol. 86, Apr. 2024, Art. no. 102679.

[4] M.-G. Kim, M. Jung, J. Hong, and K.-K.-K. Kim, "MPPI-IPDDP: A hybrid method of collision-free smooth trajectory generation for autonomous robots," *IEEE Trans. Ind. Informat.*, vol. 21, no. 7, pp. 5037–5046, Jul. 2025.

[5] A. G. Adane and C. M. Abdissa, "Adaptive fuzzy sliding mode controller of three link robot arm manipulator," *IEEE Access*, vol. 13, pp. 158222–158236, 2025.

[6] H. G. Dirara, F. T. Yareshe, and C. M. Abdissa, "Design and analysis of adaptive fuzzy super-twisting sliding mode controller for uncertain 2-DOF robotic manipulator," *IEEE Access*, vol. 13, pp. 110241–110254, 2025.

[7] G. Menyechel Eneyew, W. Ayalew Asfaw, and C. Merga Abdissa, "Optimized backstepping fuzzy sliding mode controller for trajectory tracking of mobile manipulator," *Eng. Rep.*, vol. 7, no. 7, p. 70269, Jul. 2025.

[8] T. B. Arega, Y. M. Tesfa, and C. M. Abdissa, "Three-wheeled mobile robot trajectory tracking control using nonlinear PID controller based neural network combined with backstepping controller," *IEEE Access*, vol. 13, pp. 100167–100182, 2025.

[9] F. Ostyn, T. Lefebvre, B. Vanderborght, and G. Crevecoeur, "Overload clutch design for collision tolerant high–speed industrial robots," *IEEE Robot. Autom. Lett.*, vol. 6, no. 2, pp. 863–870, Apr. 2021.

[10] J. E. Bobrow, S. Dubowsky, and J. S. Gibson, "Time-optimal control of robotic manipulators along specified paths," *Int. J. Robot. Res.*, vol. 4, no. 3, pp. 3–17, Sep. 1985.

[11] D. Kaserer, H. Gattringer, and A. Müller, "Nearly optimal path following with jerk and torque rate limits using dynamic programming," *IEEE Trans. Robot.*, vol. 35, no. 2, pp. 521–528, Apr. 2019.

[12] D. Verscheure, B. Demeulenaere, J. Swevers, J. D. Schutter, and M. Diehl, "Practical time-optimal trajectory planning for robots: A convex optimization approach," *IEEE Trans. Autom. Control*, vol. 53, no. 1, pp. 1–28, Jan. 2008.

[13] H. Pham and Q.-C. Pham, "A new approach to time-optimal path parameterization based on reachability analysis," *IEEE Trans. Robot.*, vol. 34, no. 3, pp. 645–659, Jun. 2018.

[14] Q.-C. Pham, "A general, fast, and robust implementation of the time-optimal path parameterization algorithm," *IEEE Trans. Robot.*, vol. 30, no. 6, pp. 1533–1540, Dec. 2014.

[15] V. Petrone, E. Ferrentino, and P. Chiacchio, "Time-optimal trajectory planning with interaction with the environment," *IEEE Robot. Autom. Lett.*, vol. 7, no. 4, pp. 10399–10405, Oct. 2022.

[16] Y. Fang, J. Qi, J. Hu, W. Wang, and Y. Peng, "An approach for jerk-continuous trajectory generation of robotic manipulators with kinematical constraints," *Mechanism Mach. Theory*, vol. 153, Nov. 2020, Art. no. 103957.

[17] D. K. Thomsen, R. S. Knudsen, D. Brandt, O. Balling, and X. Zhang, "Generating vibration free rest-to-rest trajectories for configuration dependent dynamic systems via 3-segmented input shaping," in *Proc. IEEE Int. Conf. Robot. Autom. (ICRA)*, May 2018, pp. 4361–4366.

[18] H. Pham and Q.-C. Pham, "On the structure of the time-optimal path parameterization problem with third-order constraints," in *Proc. IEEE Int. Conf. Robot. Autom. (ICRA)*, May 2017, pp. 679–686.

[19] L. Consolini and M. Locatelli, "Is time-optimal speed planning under jerk constraints a convex problem?," *Automatica*, vol. 169, Nov. 2024, Art. no. 111864.

[20] L. Consolini, M. Locatelli, and A. Minari, "A sequential algorithm for jerk limited speed planning," *IEEE Trans. Autom. Sci. Eng.*, vol. 19, no. 4, pp. 3192–3209, Oct. 2022.

[21] A. Palleschi, M. Garabini, D. Caporale, and L. Pallottino, "Time-optimal path tracking for jerk controlled robots," *IEEE Robot. Autom. Lett.*, vol. 4, no. 4, pp. 3932–3939, Oct. 2019.

[22] H. Huang, H. Liu, C. Xia, H. Mei, X. Gao, and B. Liang, "Sampling-based time-optimal path parameterization with jerk constraints for robotic manipulation," *Robot. Auto. Syst.*, vol. 170, Dec. 2023, Art. no. 104530.

[23] J.-W. Ma, S. Gao, H.-T. Yan, Q. Lv, and G.-Q. Hu, "A new approach to time-optimal trajectory planning with torque and jerk limits for robot," *Robot. Auto. Syst.*, vol. 140, Jun. 2021, Art. no. 103744.

[24] F. Debrouwere et al., "Time-optimal path following for robots with trajectory jerk constraints using sequential convex programming," in *Proc. IEEE Int. Conf. Robot. Autom.*, May 2013, pp. 1916–1921.

[25] S. Zhao et al., "Sigmoid angle-arc curves: Enhancing robot time-optimal path parameterization for high-order smooth motion," *Robot. Computer-Integrated Manuf.*, vol. 92, Apr. 2025, Art. no. 102884.

[26] J. Yang, D. Li, C. Ye, and H. Ding, "An analytical C^3 continuous tool path corner smoothing algorithm for 6R robot manipulator," *Robot. Comput.-Integr. Manuf.*, vol. 64, Aug. 2020, Art. no. 101947.